C. R. Physique 19 (2018) 285–305

Contents lists available at ScienceDirect

Comptes Rendus Physique

www.sciencedirect.com

Grand Prix Servant 2017 de l'Académie des sciences

Artificial graphenes: Dirac matter beyond condensed matter

Graphènes artificiels : matière de Dirac au-delà de la matière condensée

Gilles Montambaux

Laboratoire de physique des solides, CNRS, Université Paris-Sud, Université Paris-Saclay, 91405 Orsay, France

ARTICLE INFO

Article history:
Available online 7 November 2018

Keywords:
Graphene
Ultracold atoms
Microwaves
Polaritons
Phosphorene
Bloch oscillations

Mots-clés :
Graphène
Atomes ultra-froids
Micro-ondes
Polaritons
Phosphorène
Oscillations de Bloch

ABSTRACT

After the discovery of graphene and of its many fascinating properties, there has been a growing interest for the study of "artificial graphenes". These are totally different and novel systems that bear exciting similarities with graphene. Among them are lattices of ultracold atoms, microwave or photonic lattices, "molecular graphene" or new compounds like phosphorene. The advantage of these structures is that they serve as new playgrounds for measuring and testing physical phenomena that may not be reachable in graphene, in particular the possibility of controlling the existence of Dirac points (or Dirac cones) existing in the electronic spectrum of graphene, of performing interference experiments in reciprocal space, of probing geometrical properties of the wave functions, of manipulating edge states, etc. These cones, which describe the band structure in the vicinity of the two connected energy bands, are characterized by a topological "charge". They can be moved in the reciprocal space by appropriate modification of external parameters (pressure, twist, sliding, stress, etc.). They can be manipulated, created or suppressed under the condition that the total topological charge be conserved. In this short review, I discuss several aspects of the scenarios of merging or emergence of Dirac points as well as the experimental investigations of these scenarios in condensed matter and beyond.

© 2018 Published by Elsevier Masson SAS on behalf of Académie des sciences. This is an open access article under the CC BY-NC-ND license (http://creativecommons.org/licenses/by-nc-nd/4.0/).

RÉSUMÉ

Après la découverte du graphène et de ses nombreuses propriétés fascinantes, l'étude des « graphènes artificiels » suscite un intérêt croissant. Ce sont des systèmes totalement différents et nouveaux, qui présentent des similitudes intéressantes avec le graphène. Parmi eux, on trouve des réseaux d'atomes ultra-froids, des réseaux micro-ondes ou photoniques, du « graphène moléculaire » ou de nouveaux composés comme le phosphorène. L'avantage de ces structures est qu'elles servent de nouveaux terrains pour mesurer et tester les phénomènes physiques inaccessibles dans le graphène, notamment la possibilité de contrôler l'existence de points de Dirac (ou cônes de Dirac) existant dans le spectre électronique du graphène, d'effectuer des expériences d'interférence dans l'espace réciproque, de sonder les propriétés géométriques des fonctions d'onde, de manipuler des états de bord, etc. Ces cônes, qui décrivent la structure de la bande au voisinage des deux bandes d'énergie connectées, sont caractérisés par une « charge » topologique. Ils peuvent être déplacés dans l'espace réciproque par une modification appropriée des paramètres externes (pression, torsion, glissement, contrainte, etc.). Ils peuvent être manipulés, créés

E-mail address: gilles.montambaux@u-psud.fr.

https://doi.org/10.1016/j.crhy.2018.10.010
1631-0705/© 2018 Published by Elsevier Masson SAS on behalf of Académie des sciences. This is an open access article under the CC BY-NC-ND license (http://creativecommons.org/licenses/by-nc-nd/4.0/).

ou supprimés à condition que la charge topologique totale soit conservée. Dans cette brève revue, je discute plusieurs aspects des scénarios de fusion ou d'émergence de points de Dirac ainsi que des investigations expérimentales de ces scénarios dans la matière condensée et au-delà.

© 2018 Published by Elsevier Masson SAS on behalf of Académie des sciences. This is an open access article under the CC BY-NC-ND license (http://creativecommons.org/licenses/by-nc-nd/4.0/).

1. Introduction

Graphene is a two-dimensional solid constituted by a single layer of graphite, in which the carbon atoms are arranged in a regular honeycomb structure. One of the main interests of this "wonder material" [1,2] isolated in 2004 is its very unusual electronic spectrum: Fig. 1 presents the energy $\epsilon(\boldsymbol{k})$ of an electronic state as a function of the electron momentum $\boldsymbol{k}$, a two-dimensional vector of the reciprocal lattice. As will be reminded in section 2, it consists in two bands touching at two singular points, named $\boldsymbol{K}$ and $\boldsymbol{K}'$, of the Brillouin zone. Around these points the spectrum is linear. These singularities are well described by the Dirac equation for massless particles in two dimensions. For this reason, these special points of the reciprocal space are usually called *Dirac points* and the associated cones are called *Dirac cones*. The term *Dirac matter* is frequently used to characterize newly discovered condensed matter systems having electronic properties described by a Dirac-like equation [3].

Even more important is the structure of the electron wave functions. The graphene honeycomb lattice consists in a hexagonal Bravais lattice[1] with an elementary pattern made of two inequivalent sites named A and B (Fig. 2). Therefore in the tight-binding approximation, the wave function has two components corresponding to its amplitude on A and B sites. The relative phase between these two components depends on the position of the momentum $\boldsymbol{k}$, that is, the position of the state in the Brillouin zone, see section 2. Near the Dirac points, this phase has a special structure: it winds around each point and the winding is opposite ($2w\pi$ with $w = \pm 1$) for the two Dirac points (Fig. 1). Since the winding is a topological property, the Dirac points behave as topological charges in the reciprocal space. These two charges w have opposite signs. It is then natural to ask the question whether these two charges may be moved and even be annihilated. The theoretical and experimental answers to this question are the subject of this work. It has been proposed that the merging of a pair of such Dirac points follows a universal scenario, in the sense that it does not depend on the microscopic problem considered: it describes as well the dynamics of electrons as other waves like microwaves, light or matter waves, that is, far beyond the field of graphene or even of condensed matter [4].

Such annihilation of Dirac points is not reachable in graphene because it would imply a large deformation of the lattice impossible to achieve [5,6]. However, it may be observed in various different physical systems, including several beyond condensed matter, which share common properties or interesting analogies with graphene. Such systems are now called "artificial graphenes". The list of such systems is now very long and has been reviewed in a recent paper [7]. In the present paper, we will not address the huge literature on the subject, but only restrict ourselves to several realizations of artificial graphenes in which the motion and merging of Dirac points has been achieved and studied.

The outline of this paper is as follows: we first start with a brief introduction to the electronic properties of graphene. Then we show that the motion and merging of Dirac points follows a universal scenario with a peculiar spectrum at the merging transition: it is quadratic along one direction and linear in the perpendicular direction. This peculiar structure of the spectrum, named semi-Dirac, is accompanied by the annihilation of the windings numbers attached to the Dirac points, signature of the topological character of the transition [8]. In the next sections, we consider several experimental works in which this transition has been observed. We emphasize that each experimental situation is not a simple reproduction of graphene physics, but either allows for the investigation of situations not reachable in graphene or opens new directions of research proper to this situation. We conclude by a generalization to various mechanisms of merging of Dirac points.

2. Brief reminder about graphene

The valence and conduction bands of graphene are described by a simple tight-binding Hamiltonian

$$\mathcal{H} = -t \sum_{j,j'} |\varphi_j^{\mathrm{A}}\rangle\langle\varphi_{j'}^{\mathrm{B}}| + h.c. \tag{1}$$

where the parameter t characterizes the hopping between nearest neighboring sites. Additional hoppings between higher nearest neighbors exist, but are omitted here, since they do not change much the physics and do not affect the geometric structure of the wave functions. Here we choose to write the eigenfunctions in the form

$$\psi_{\boldsymbol{k}}(\boldsymbol{r}) = \mathrm{e}^{\mathrm{i}\boldsymbol{k}\cdot\boldsymbol{R}} u_{\boldsymbol{k}}(\boldsymbol{r}) \tag{2}$$

[1] Also sometimes called triangular.

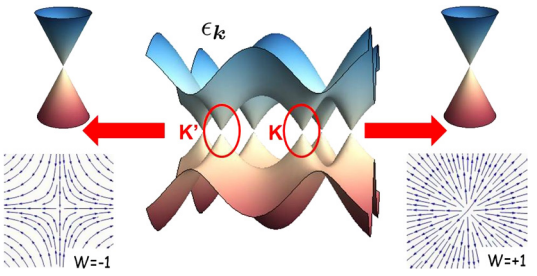

Fig. 1. Top: the energy spectrum $\epsilon(\boldsymbol{k})$ exhibits two inequivalent points K and K′ where the dispersion relation is linear. Bottom: representation of the vector field $(\cos\phi_{\boldsymbol{k}}, \sin\phi_{\boldsymbol{k}})$, where $\phi_{\boldsymbol{k}}$ is the relative phase between the two components of the wave function. The winding of the wave function around K and K′ is characterized by a winding number $w = \pm 1$.

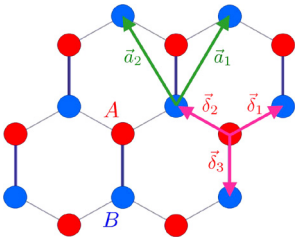

Fig. 2. The "honeycomb" lattice consists in an hexagonal Bravais lattice and two atoms per unit cell. We have represented the elementary vectors $\boldsymbol{a}_1, \boldsymbol{a}_2$ of the Bravais lattice and the three vectors $\boldsymbol{\delta}_1, \boldsymbol{\delta}_2, \boldsymbol{\delta}_3$ connecting one site to its nearest neighbors.

where the function $u_{\boldsymbol{k}}(\boldsymbol{r})$ has the periodicity of the real Bravais lattice *and* of the reciprocal lattice (see discussion about this second statement in Appendix A),

$$u_{\boldsymbol{k}}(\boldsymbol{r}+\boldsymbol{R}) = u_{\boldsymbol{k}}(\boldsymbol{r}) \qquad , \qquad u_{\boldsymbol{k}+\boldsymbol{G}}(\boldsymbol{r}) = u_{\boldsymbol{k}}(\boldsymbol{r}) \tag{3}$$

$\boldsymbol{R}$ is a vector of the Bravais lattice and $\boldsymbol{G}$ is a vector of the reciprocal lattice. In the tight-binding approximation, the cell-periodic part $u_{\boldsymbol{k}}$ is only defined on A and B sites and it is solution to $\mathcal{H}_{\boldsymbol{k}} u_{\boldsymbol{k}} = E_{\boldsymbol{k}} u_{\boldsymbol{k}}$ with the effective Hamiltonian

$$\mathcal{H}_{\boldsymbol{k}} = \begin{pmatrix} 0 & f_{\boldsymbol{k}} \\ f_{\boldsymbol{k}}^* & 0 \end{pmatrix} \tag{4}$$

and

$$f_{\boldsymbol{k}} = -t(1 + \mathrm{e}^{\mathrm{i}\boldsymbol{k}\cdot\boldsymbol{a}_1} + \mathrm{e}^{\mathrm{i}\boldsymbol{k}\cdot\boldsymbol{a}_2}) \,, \tag{5}$$

where $\boldsymbol{a}_1$ and $\boldsymbol{a}_2$ are elementary vectors of the Bravais lattice (Fig. 2). The solutions are

$$u_{\boldsymbol{k}} = \frac{1}{\sqrt{2}} \begin{pmatrix} 1 \\ \pm \mathrm{e}^{\mathrm{i}\phi_{\boldsymbol{k}}} \end{pmatrix} \tag{6}$$

with the relative phase $\phi_{\boldsymbol{k}} = \arg(f_{\boldsymbol{k}}^*)$. They are associated with the energies $\epsilon_{\boldsymbol{k}} = \pm|f_{\boldsymbol{k}}|$ represented in Fig. 1. The spectrum exhibits two bands touching linearly in two inequivalent points of the Brillouin zone. In the vicinity of these two "Dirac points", the Hamiltonian (4) takes the linear form:

$$\mathcal{H}_{\boldsymbol{k}} = c \begin{pmatrix} m\,c & \hbar\,(\pm q_x - \mathrm{i}\,q_y) \\ \hbar\,(\pm q_x - \mathrm{i}\,q_y) & -m\,c \end{pmatrix} \tag{7}$$

where $\boldsymbol{q} = \boldsymbol{k} - \boldsymbol{K}^{(\prime)}$, $\hbar c = 3\,t\,a/2$ and $m = 0$. This is the form of the Dirac equation for massless particles ($m = 0$) in two dimensions. The energy spectrum is linear,

$$\epsilon_{\boldsymbol{q}} = \pm \hbar\, c\, |\boldsymbol{q}| \tag{8}$$

The velocity c is 300 smaller than the speed of light. The relative phase $\phi_{\boldsymbol{k}}$ is plotted in Fig. 3. The winding number around a contour C in the reciprocal space is defined as [9]

$$w(C) = \frac{1}{2\pi} \oint_C \nabla\phi_{\boldsymbol{k}} \cdot \mathrm{d}\boldsymbol{k} \tag{9}$$

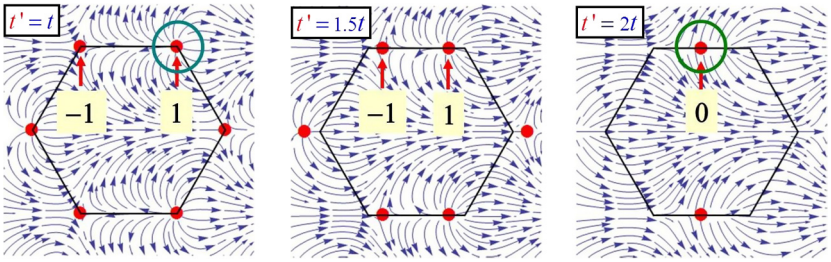

Fig. 3. Evolution of the dependence $\phi_{\boldsymbol{k}}$ from the isotropic case $t' = t$ to the merging topological transition $t' = 2t$. At the transition, the opposite winding numbers annihilate. These figures represent the vector field $(\cos\phi_{\boldsymbol{k}}, \sin\phi_k)$.

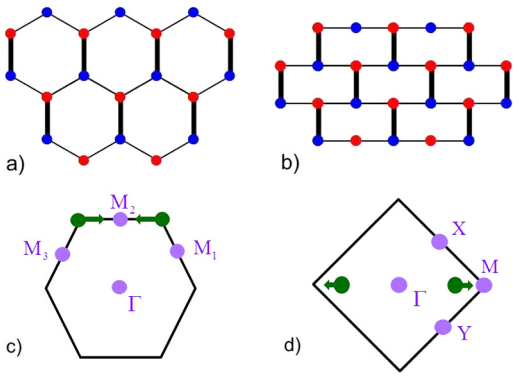

Fig. 4. Top: honeycomb (a) and brickwall (b) lattices. Bottom: position (green dots) of the Dirac points for the isotropic honeycomb and brickwall lattices. Their merging can occur at one of the four TRIMs pictured (purple dots) in the first Brillouin zones for the honeycomb (c) and the brickwall (d) lattices.

The two Dirac points are characterized by opposite winding numbers $w = \pm 1$. One important physical signature of this winding structure concerns the Landau levels spectrum ϵ_n obtained from the semi-classical Onsager relation [10]

$$N(\epsilon_n) = (n + \gamma)\frac{e\,B}{h} \tag{10}$$

where $e\,B/h$ is the degeneracy of a Landau level and $N(\epsilon)$ is the number of states below energy ϵ, that is, the integral of the density of states (these quantities are written by unit area). The phase factor $\gamma = 1/2 - w(C)/2$ contains the usual Maslov index $1/2$ of the harmonic oscillator and the winding number [11,12]. In the vicinity of the Dirac points, the spectrum being linear, the density of states is also linear ($= \epsilon/\hbar^2 c^2$). Application of the Onsager formula leads to a sequence of Landau levels given by [2]

$$\epsilon_n(B) = \pm c\sqrt{2n\hbar e\,B} \qquad , \qquad n \in \mathbb{N} \tag{11}$$

The observation of this sequence of levels and, in particular, the existence of a zero-energy level were one of the first signatures, not only of the strictly 2D character of graphene, but also of the spinorial character of the wave functions and of the Dirac-like structure of the electronic equation of motion [13].

3. Motion and merging of Dirac points

3.1. A toy model

It is first instructive to consider a toy model that consists in a slight variation of the graphene model [4,14–16]. One of the three hopping parameters introduced in Eq. (5) is now fixed to a different value $t' > t$ (the vertical bars in Fig. 4). The function $f_{\boldsymbol{k}}$ defined above is now given by

$$f_{\boldsymbol{k}} = -(t' + t\,e^{i\boldsymbol{k}\cdot\boldsymbol{a}_1} + t\,e^{i\boldsymbol{k}\cdot\boldsymbol{a}_2}) \tag{12}$$

The position of the Dirac points being given by $f_{\boldsymbol{k}} = 0$, it is easy to check, and this is shown in Fig. 5, that when the parameter t' increases, the Dirac points move until they merge at the M_2 point (as defined in Fig. 4c). This happens for the critical value of the merging parameter $\beta \equiv t'/t = 2$. Above this value, $f_{\boldsymbol{k}} = 0$ has no solution, implying the existence of a gap in the energy spectrum. The evolution of the spectrum is shown in Fig. 5: when t' increases, the two Dirac points tend to approach each other, the velocity along the merging line decreases until it vanishes at the transition $t' = 2t$. At

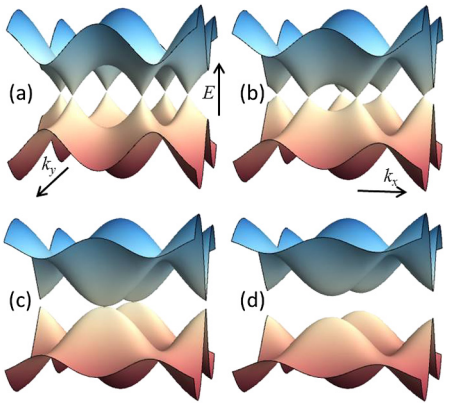

Fig. 5. Evolution of the energy spectrum for the toy model (4), (12), with $\beta = t'/t = 1(a), 1.5(b), 2\ (c), 2.5\ (d)$. At the critical value $\beta = 2$, the spectrum is semi-Dirac.

the transition, the spectrum is quite interesting, it is quadratic along the direction of merging, but stays linear along the perpendicular direction. More precisely, it has the form

$$\epsilon(\boldsymbol{q}) = \pm\sqrt{\left(\frac{q_x^2}{2m_*}\right)^2 + c^2 q_y^2} \tag{13}$$

where $m_* = 2/(3ta^2)$ and $c = 3ta$ ($\hbar = 1$). This hybrid spectrum, massive–massless, has been baptized "semi-Dirac" [17]. This critical spectrum corresponds to a *topological Lifshitz transition* [8], since the two winding numbers associated with the Dirac points have annihilated and the winding number around the point M is now 0. At this point and in its vicinity, the thermodynamic and transport properties are quite new [4,15,18]. The density of states associated with this hybrid spectrum scales as $\sqrt{\epsilon}$ and, since the winding number is zero, the Onsager–Roth formula leads to a dependence of the Landau levels of the form $\epsilon_n(B) \propto [(n+1/2)B]^{2/3}$ [15].

3.2. A universal Hamiltonian

A natural question now arises whether this toy model is generic of more general situations. We have shown that this scenario of merging is actually quite general [4]. The demonstration is as follows. Consider a general situation where objects (these can be atoms, molecules, classical wave scatterers, semiconducting micropillars, etc.) on a lattice are described by a Hamiltonian whose general structure is given in Eq. (4). The function f describes the coupling between A and B sites. Quite generally, the function $f_{\boldsymbol{k}}$ can be written in the form (this function has the periodicity of the reciprocal lattice, see Appendix A):

$$f_{\boldsymbol{k}} = \sum_{m,n} t_{mn} \mathrm{e}^{\mathrm{i}\boldsymbol{k}\cdot\boldsymbol{R}_{mn}} \tag{14}$$

where $\boldsymbol{R}_{mn}$ are vectors of a Bravais lattice. For example, in the previous toy model, we have simply $t_{00} = t'$, $t_{01} = t_{10} = t$ and other parameters $t_{mn} = 0$. In general, depending on the values of these parameters, there may be either no Dirac point, one or several pairs $(\boldsymbol{D}, -\boldsymbol{D})$ of Dirac points. The merging of two partners necessarily occurs when $\boldsymbol{D} = -\boldsymbol{D}\ (\mathrm{mod}\, \boldsymbol{G}^{pq})$ where $\boldsymbol{G}^{pq} = p\boldsymbol{a}_1^* + q\boldsymbol{a}_2^*$ is a reciprocal lattice vector. Therefore, merging occurs at points $\boldsymbol{D}^{pq} = \boldsymbol{G}^{pq}/2$. There are four inequivalent (they cannot be deduced from each other by a translation of a reciprocal lattice vector) such points called Time Reversal Invariant Momenta (TRIM) corresponding to $(p,q) = (0,0), (0,1), (1,0)$ or $(1,1)$. The merging of a pair of Dirac points occurs at such a point $\boldsymbol{D}^{pq}$ when the parameter $f_{\boldsymbol{D}^{pq}} = \sum_{m,n} t_{mn} \mathrm{e}^{\mathrm{i}\boldsymbol{D}^{pq}\cdot\boldsymbol{R}_{mn}}$ vanishes. Since the product $\boldsymbol{G}^{pq}\cdot\boldsymbol{R}_{mn} = 2\pi(pm+qn)$, this parameter is given by $f_{\boldsymbol{D}^{pq}} = \sum_{m,n} t_{mn}\beta_{mn}^{pq}$, where we have defined $\beta_{mn}^{pq} = (-1)^{pm+qn}$. In the previous example, for graphene, merging at the M_2 point $(p=1, q=1)$ occurs when the parameter $f_{\boldsymbol{D}^{pq}} = t_{00} - t_{01} - t_{10} = t' - 2t$ vanishes.

Let us now consider the vicinity of this merging point by an expansion of the wave vector. Writing $\boldsymbol{k} = \boldsymbol{D}^{pq} + \boldsymbol{q}$, we find

$$f_{\boldsymbol{D}^{pq}+\boldsymbol{q}} = f_{\boldsymbol{D}^{pq}} + \mathrm{i}\,\boldsymbol{q}\cdot\sum_{mn}\beta_{mn}^{pq} t_{mn}\boldsymbol{R}_{mn} - \frac{1}{2}\sum_{mn}\beta_{mn}^{pq} t_{mn}(\boldsymbol{q}\cdot\boldsymbol{R}_{mn})^2 + \cdots \tag{15}$$

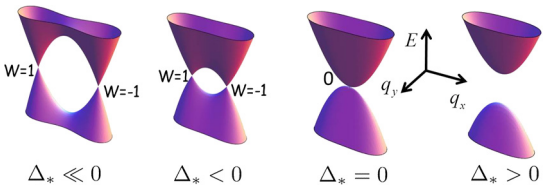

Fig. 6. Universal scenario for the merging transition between the Dirac phase ($\Delta_* < 0$) and the gapped phase ($\Delta_* > 0$).

The linear term is *purely imaginary*. It defines a direction $\hat{y}$ and a velocity

$$c^{pq} = \sum_{m,n} \beta_{mn}^{pq} t_{mn} R_{y,mn} \tag{16}$$

Once this local axis is defined, consider the quadratic terms. They are of the form $q_x^2, q_x q_y, q_y^2$, where $\hat{x}$ is defined as the direction perpendicular to $\hat{y}$. At the lowest order, we keep only the term q_x^2. Then the function $f_{\boldsymbol{D}^{pq}+\boldsymbol{q}}$ has the expansion

$$f_{\boldsymbol{D}^{pq}+\boldsymbol{q}} = f_{\boldsymbol{D}^{pq}} + \mathrm{i}\, c^{pq} q_y + \frac{q_x^2}{2m^{pq}} \tag{17}$$

Of course, the parameters c^{pq}, m^{pq} and Δ^{pq} depend on the position (p,q) of the merging point, and they will be now simply denoted by c, m_* and Δ_*. The effective mass m_* and the merging parameter Δ_* are given by

$$\frac{1}{m_*} = -\sum_{mn} \beta_{mn}^{pq} t_{mn} R_{x,mn}^2 \tag{18}$$

$$\Delta_* = \sum_{mn} \beta_{mn}^{pq} t_{mn} \tag{19}$$

We conclude that, in the vicinity of the merging point at a TRIM, the Hamiltonian as the *universal form*

$$\mathcal{H}(\boldsymbol{q}) = \begin{pmatrix} 0 & \Delta_* + \frac{q_x^2}{2m_*} + \mathrm{i}\, c\, q_y \\ \Delta_* + \frac{q_x^2}{2m_*} - icq_y & 0 \end{pmatrix} \tag{20}$$

where the parameters depend on the position of the merging point. In addition to being independent of the details of the microscopic parameters, we stress that this is the minimal Hamiltonian that describes the coupling between two Dirac points of opposites charges and their merging [4]. The dispersion relation given by

$$\epsilon(\boldsymbol{q}) = \pm \sqrt{\left(\Delta_* + \frac{q_x^2}{2\,m_*}\right)^2 + c^2 q_y^2} \tag{21}$$

is shown in Fig. 6. When $\Delta_* < 0$, it describes a pair of massless Dirac points with opposite winding numbers [4]. The two Dirac points at positions $\pm\sqrt{-2m^*\Delta_*}$ are separated by a saddle point (Van Hove singularity) at energy $|\Delta_*|$. At the critical value $\Delta_* = 0$, the spectrum has the hybrid "semi-Dirac" form, quadratic in the $\hat{x}$ direction and linear in the $\hat{y}$ direction. The density of states associated with this hybrid spectrum scales as $\sqrt{\epsilon}$. When $\Delta_* > 0$, a gap opens. The Hamiltonian (20) describes a continuous cross-over between the limit of uncoupled valleys corresponding to the situation in graphene and the merging of the Dirac points. It allows for a continuous description of the coupling between valleys, which increases as the energy of the saddle point decreases.

In Refs. [4,15,18], we have studied the thermodynamic and transport properties of this Hamiltonian, in particular the spectrum in a magnetic field. The evolution of the Landau levels from the Dirac phase $\Delta_* < 0$ to the gapped phase $\Delta_* > 0$ is shown in Fig. 7. In the Dirac phase, the Landau levels vary as $\sqrt{nB}$ (Eq. (11)) with a double valley degeneracy. When the energy of the Landau levels reaches the energy of the saddle point $|\Delta_*|$, the two-fold valley degeneracy is lifted. At the critical value $\Delta_* = 0$, the energy levels scale as $[n + (1/2)B]^{2/3}$, a consequence of the $\sqrt{\epsilon}$ dependence of the density of states and of the cancellation of the winding number. Above the transition, in the gapped phase, one recovers usual Landau levels varying linearly with the field.

In Ref. [4], it was proposed a slightly more general toy model than the one presented above. It consists of a lattice with four different hopping parameters $t_{00}, t_{01}, t_{10}, t_{11}$. In this case, the merging parameter Δ_* depends on the merging point (one of the four TRIMs) and it is given by Eq. (19), that is,

$$\Delta_* = t_{00} + (-1)^p t_{01} + (-1)^q t_{10} + (-1)^{p+q} t_{11} \tag{22}$$

Put it differently, the merging or emergence of Dirac points is possible at the TRIM (p,q) where this parameter vanishes. Fig. 8 shows the motion of the Dirac points between the four different TRIMs under appropriate variation of hopping

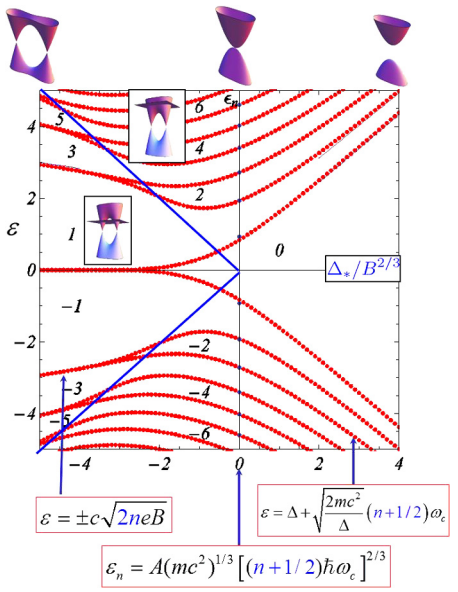

Fig. 7. Evolution of the Landau spectrum as a function of the parameter $\Delta^*/B^{2/3}$. The sequence of Hall numbers is indicated in the gaps. The blue line corresponds to the energy of the saddle point separating Dirac cones. For more details, see Ref. [4].

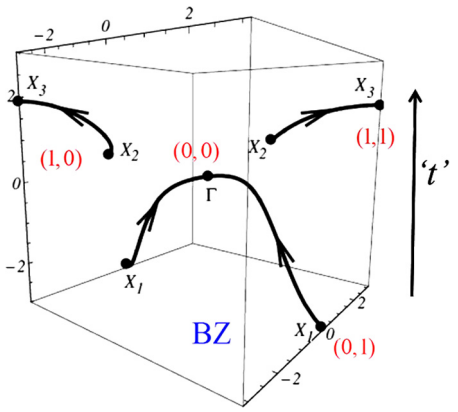

Fig. 8. Motion of Dirac points when varying the parameters of Eq. (22). Here 't' represents a variation of the hopping parameters that is not detailed here. See Ref. [4] for the choice of parameters.

parameters. We shall see in the next section that this tight-binding model has been achieved experimentally. The particular choice of parameters $t_{00} = t'$, $t_{01} = t_{10} = t$, $t_{11} = 0$ corresponds to the "brickwall" lattice, very similar to graphene, but with a rectangular symmetry, see Figs. 4 and 9.

The scenario described by the universal Hamiltonian was proposed in 2009. It was immediately realized that the merging of Dirac points could not be reached in graphene, because it would need an applied strain along one direction of about 23% [5,6]. This scenario remained considered as a theoretical exercise for a few years. It was predicted to be accessible in the organic conductor α-(BEDT–TTF)$_2$I$_3$ under high pressure, but has not been observed yet [19]. It took a few years to highlight this scenario in various systems emulating the physics of electronic propagation in graphene. These systems are now called "artificial graphenes". Their interest lies in the strong experimental challenge for their realization and the variety of physical questions they raise. In the next sections, we detail several experiments on artificial graphenes in which the motion and merging of Dirac points have been highlighted.

4. Cold atoms

electrons $\longrightarrow$ atoms

atomic lattice $\longrightarrow$ optical lattice

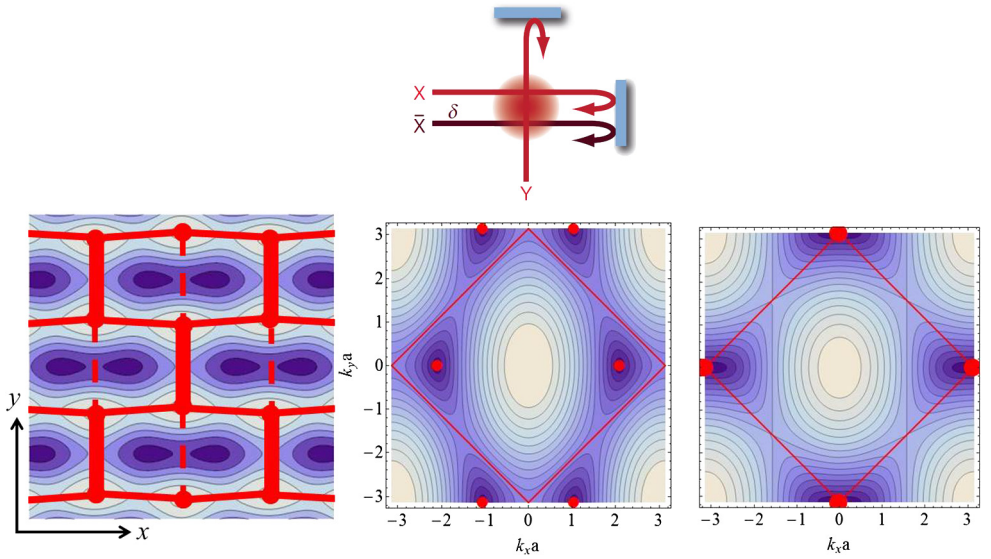

Fig. 9. Top: three lasers beams create a two-dimensional potential (see Ref. [20] for details). Bottom left: spatial dependence of this optical potential described by a tight-binding model. The atomic sites correspond to the minima of the potential (light blue) Tunneling is avoided along the maxima of the potential (dark blue). The lines represent the hopping amplitudes (t: horizontal lines, t': thick vertical lines, t'': dashed vertical lines). Bottom right: isoenergy lines and position of the Dirac points for $t' = t$ and $t' = 2t$ ($t'' = 0$).

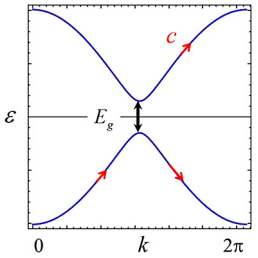

Fig. 10. A atom initially in the lower band submitted to a constant force F may tunnel from the lower to the upper band.

In condensed matter, the structure of the atomic orbitals makes it impossible to realize a brickwall lattice. However, such a lattice can be achieved with ultracold atoms trapped in an optical lattice [20]. An appropriate potential profile, schematized in Fig. 9, is generated with three stationary laser beams. With appropriate laser intensities (denoted by V_X and $V_{\overline{X}}$, see Fig. 9 and Ref. [20]), the energy spectrum of the trapped atoms exhibits two bands with a pair of Dirac points, well described by the brickwall tight-binding model with essentially two parameters t and t', which can be tuned by modification of the laser parameters. A third parameter t'' may be introduced for a better quantitative modeling (Fig. 9). The motion and merging of these points are properly tuned by variation of the laser parameters. In order to probe the spectrum and its evolution, a low-energy cloud of fermionic atoms ^{40}K occupies the bottom of the lower band and is submitted to a constant force F inducing a linear time dependence $\hbar k = F t$ of the quasi-momentum $\boldsymbol{k}$, so that the energy $\epsilon(\boldsymbol{k})$ oscillates with time. This phenomenon is called a Bloch oscillation [21,22]. If the motion is slow (small F), a state $k(t)$ moves adiabatically along the energy band $\epsilon(k(t))$. If the motion is fast (large F) and when two bands become close to each other, an atom initially in the lower band has a finite probability to tunnel to the upper band. Near a Dirac point, the tunneling probability is given by the Landau–Zener–Stückelberg theory and is related to the gap E_g between the two bands: [23]

$$P_Z = \mathrm{e}^{-\pi \frac{(E_g/2)^2}{c\,F}} \tag{23}$$

F is the force that drives the linear time dependence of the wave vector k and c is the velocity (Fig. 10). By measuring the proportion of atoms transferred to the upper band after a single Bloch oscillation, it is possible to reconstruct the energy spectrum in the vicinity of the Dirac points, therefore to highlight the motion and merging of Dirac points under the effect of a distortion of the lattice induced by appropriate variations of the laser parameters. Two geometries are of interest, when the force is applied along or perpendicularly to the merging line (Fig. 11a, d).

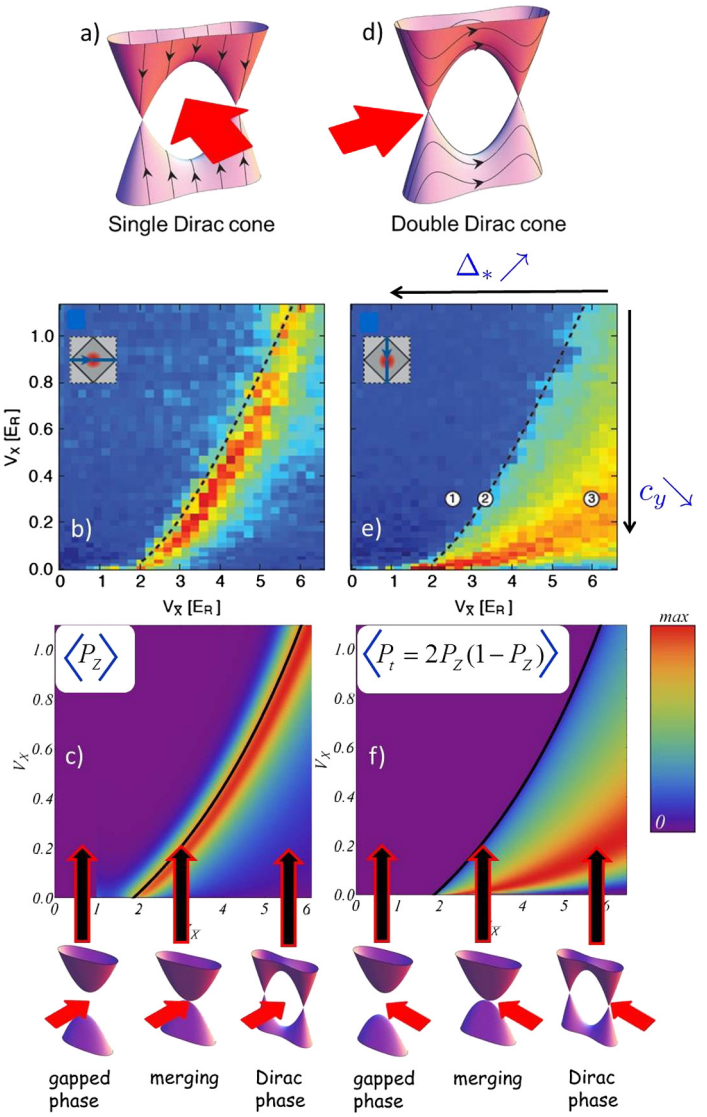

Fig. 11. A low-energy fermionic cloud of cold atoms is accelerated towards a pair of Dirac points (a, b). The probability to tunnel to the upper band depends on the vicinity of the Dirac cones. This probability is represented as a function of the two laser parameters V_X and $V_{\overline{X}}$, see Refs. [20,24]. Top figures b, e: experimental results [20]. The dashed line indicates the merging transition (2) separating the gapped phase (1) and the Dirac phase (3). Figures c, f: theory [24]. After a single Zener tunneling event, the probability is maximal close to the merging line (left figures). When a double Zener tunneling, the probability in maximal inside the Dirac phase.

4.1. Single Zener tunneling

In this first situation, the force F in applied along the $\hat{y}$-direction perpendicular to the merging line so that the fermionic cloud hits the two Dirac points in parallel (Fig. 11a). An atom in a state with finite q_x performs a Bloch oscillation along a direction of constant q_x and may tunnel into the upper band with the probability

$$P_Z^y = \mathrm{e}^{-\pi \frac{(\Delta_* + \frac{q_x^2}{2m^*})^2}{c_y F}} \tag{24}$$

In the gapped (G) phase ($\Delta_* > 0$), the tunneling probability is vanishingly small. Deep in the Dirac (D) phase ($\Delta_* < 0$), when the distance between the two Dirac points $2q_D = 2\sqrt{2m_*|\Delta_*|}$ is larger than the size of the cloud, the tunnel probability is also small (Fig. 11b). It is maximal close to the merging transition. In order to simulate the finite width of the fermionic cloud, the probability (24) has to be averaged over a finite range of q_x. Then the three parameters of the universal Hamiltonian can be related to the tight-binding parameters and then, via a simple *ab initio* calculation, to the two parameters $(V_X, V_{\overline{X}})$ of the optical potential to finally obtain the probability as a function of these two parameters. As shown in

Fig. 11, we have found that the laser amplitude $V_{\overline{X}}$ mainly tunes the merging parameter Δ_* while the laser amplitude V_X essentially tunes the velocity c_y. One obtains, without adjustable parameter, an excellent agreement with the experimental result (compare Figs. 11b and c) [24]. In particular, we find that the probability is maximal for $\Delta_* \simeq -\langle q_x^2\rangle/2m_*$, that is, *inside* the Dirac phase, as found experimentally.

4.2. Double Zener tunneling

The force F is now applied along the merging direction $\hat{x}$ so that the fermionic cloud hits the two Dirac points in series (Fig. 11d). Along one Bloch oscillation, an atom of fixed q_y performs now two Zener transitions in a row, each of them being characterized by the tunnel probability

$$P_Z^x = \mathrm{e}^{-\pi\frac{c_y^2 q_y^2}{c_x F}} = \mathrm{e}^{-\pi\frac{c_y^2 q_y^2}{F\sqrt{2|\Delta_*|/m_*}}} \tag{25}$$

Assuming that the two tunneling events are incoherent, the total interband transition probability is

$$P_t^x = 2P_Z^x(1-P_Z^x) \tag{26}$$

In the gapped phase, the tunneling probability is again vanishingly small. In the Dirac phase, the interband transition probability [Eq. (26)] is a non-monotonic function of the Zener probability P_Z^x, and it is maximal when $P_Z^x = 1/2$. This explains why the maximum of the tunnel probability is located well *inside* the D phase (red region in Figs. 11e, f). Again, after averaging over q_y, the size of the initial cloud, and relating the parameters Δ_*, m_* and c_y to the microscopic parameters $(V_X, V_{\overline{X}})$, one finds an excellent agreement with the experimental result (compare Figs. 11e and f).

4.3. Interferometry in the reciprocal space

The double Zener configuration is particularly interesting because of possible interference between the two Zener events. Assuming that the phase coherence is preserved, instead of the probability given by Eq. (26), one expects a resulting probability of the form

$$P_t^x = 4P_Z^x(1-P_Z^x)\cos^2(\varphi/2+\varphi_d) \tag{27}$$

where φ_d is a phase delay, named Stokes phase, attached to the each tunneling event, and $\varphi = \varphi_\mathrm{dyn} + \varphi_\mathrm{g}$ is a phase that has two contributions, a dynamical phase φ_dyn acquired between the two tunneling events and basically related to the energy difference between the two energy paths, and a geometric phase φ_g. Whereas the dynamical phase carries information about the spectrum, the geometric phase carries information about the structure of the wave functions [25,26]. If the interference pattern could not been observed in the experiment of Ref. [20], probably because the optical lattice was actually three-dimensional, it is an experimental challenge to access it directly and to probe the different contributions to the dephasing. More recent experiments with a honeycomb lattice of ultracold atoms have permitted to completely reconstruct the full structure of the wave functions, [27,28] as expected theoretically [29].

5. Microwaves

electrons ⟶ microwaves
atomic lattice ⟶ lattice of dielectric resonators

Another artificial graphene has been simulated with a macroscopic setup where centimeter-size cylindrical dielectric dots replace carbon atoms and microwaves replace the electrons [30]. A few hundred dots are sandwiched between two metallic plates and are arranged in a 2D honeycomb lattice. A microwave is sent through this artificial crystal and is collected by an antenna. The measured signal is related to the local density of states at the place of the antenna. The global density of states is obtained from averaging on the position of the antenna. Therefore this new setup realizes a microwave analog simulator of the quantum propagation of electrons in graphene. The distance between the dots fixes the intensity of the electromagnetic coupling. The frequency of the microwave (a few GHz) is such that its propagation is resonant in the dots and is evanescent outside. Its propagation in the lattice is thus well described by the same tight-binding model as for graphene. Like in graphene, the second and third neighbor couplings are not negligible (here $t_2/t \sim -0.09$, $t_3 \simeq 0.07$). They do not alter the properties of the Dirac cones, but they change the overall shape of the density of states (Fig. 12) [31].

This setup allows for the observation of effects hardly visible or difficult to explore in graphene like the topological transition. Here it can be reached by fabricating an appropriately uniaxial strained lattice. By doing so, the hopping parameters are modified, essentially the nearest neighbor hopping t' along the strain direction. The merging parameter Δ_* is given by Eq. (19) with the additional parameters $t_{11} = t_{1,-1} = t_{-1,1} = t_3$, that is, $(p = q = 1, m = n = 1)$:

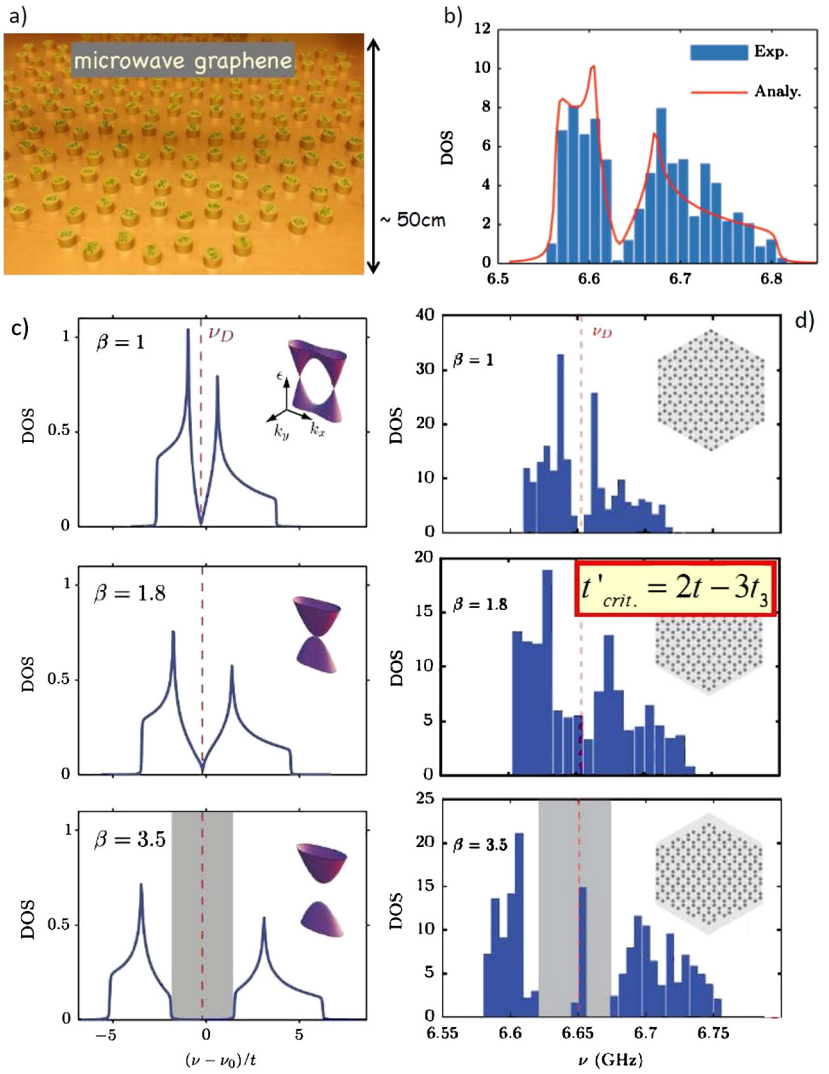

Fig. 12. a) Honeycomb lattice of 288 dielectric cylinders. b) Measured density of states well fitted by a tight-binding model with second and third nearest neighbor couplings. c) Expected evolution of the density of states when increasing the anisotropy parameter $\beta = t'/t$. d) Experimental evolution of the density of states. The merging transition occurs when $\beta = 2 - 3t_3/t$. Under strain, new edge states appear at the band center.

$$\Delta_* = t' - 2t + 3t_3 \tag{28}$$

so that the merging transition is expected for the parameter $t' = 2t - 3t_3 \simeq 1.8t$, as observed experimentally (Fig. 12).

Moreover, the simplicity of this setup allows us to probe easily the existence of new exotic states at the edges of the system. The configuration of the edges, well known to play an important role in graphene but difficult to control, is quite easy to modify here. Fig. 13 shows a lattice of dielectric dots with the three types of edges, armchair, zigzag, and bearded. The last type of edge, hard to achieve in condensed matter, is quite easy to build here. In this experiment, it has been possible to control the existence of localized states along these different edges, and to control the different types of edge states under an applied strain [32]. Moreover, it is possible to measure, for each state, the spatial repartition of the microwave field along the edges. For example, the experiment of Fig. 12 was performed on a sample with armchair edges, which are known not to support localized edge states. However, under strain along an appropriate direction, it was predicted that zero-energy localized states would appear along the armchair edges [33]. This evolution is seen in Figs. 12d and 13c.

It has been shown that the existence of zero-energy edge states can be related to a geometric property of the bulk wave functions encoded in a topological quantity bearing similarity with a Zak phase, a one-dimensional equivalent of the Berry phase [33]. First the Hamiltonian, that is the function $f_{\boldsymbol{k}}$, has to be written consistently with the type of edge, as explained in Ref. [33]. Then the topological quantity

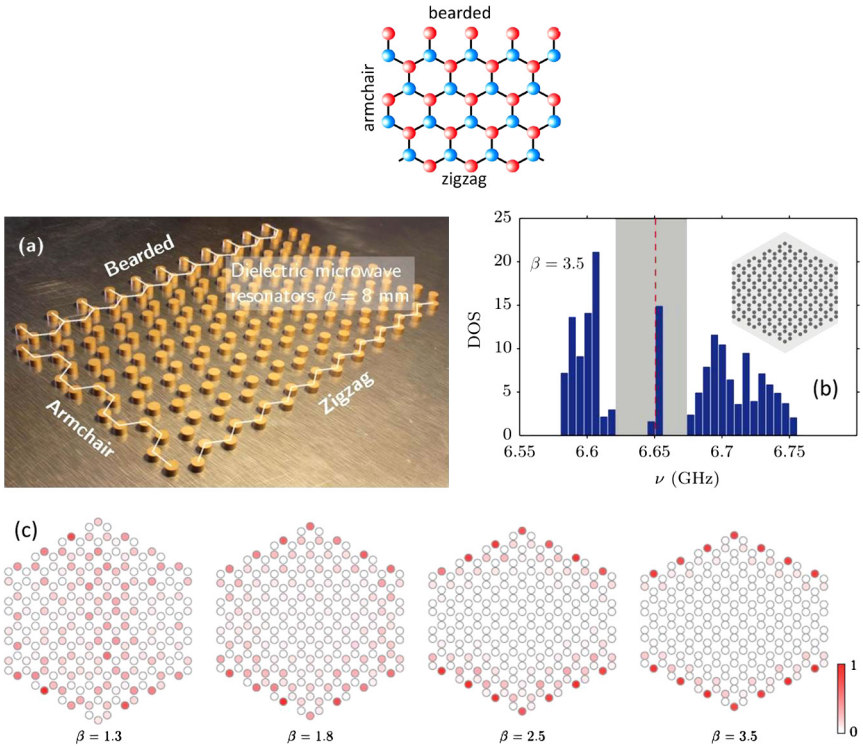

Fig. 13. a) The three types of edges, armchair, zigzag, and bearded, are achieved on this sample. b) In this lattice under strain, zero-energy localized states appear along the armchair edges. c) Evolution of the detected intensity along the armchair edges, showing the appearance of edge states [30].

$$w(k_{\parallel}) = \frac{1}{2\pi}\int \frac{\partial \phi_{\boldsymbol{k}}}{\partial k_{\perp}} \mathrm{d}k_{\perp} \tag{29}$$

measures the winding of the wave function along the direction $\perp$ perpendicular to the edges. It directly gives the number of edge states with a wave vector $k_{\parallel}$ along a given edge. Fig. 14 shows the winding of the phase and values of $k_{\parallel}$ for which zero-energy edge states exist. It can be seen that zigzag and bearded states are complementary and that a strain perpendicular to the edges modifies the relative proportion of bearded and zigzag states. When $\beta < 1$, new bearded edge states appear at the expense of zigzag edge states. On the opposite, when $\beta > 1$, new zigzag edge states appear at the expense of bearded edge states, see Fig. 14. A similar experiment has been realized in another "photonic" graphene realized with an array of waveguides arranged in the honeycomb geometry [34].

6. Polaritons

electrons $\longrightarrow$ polaritons
atomic lattice $\longrightarrow$ SC micropillars

Another very interesting setup is a honeycomb lattice of semiconducting (SC) micropillars in which polaritons propagate [35]. These mixed light–matter quasiparticles arise from the strong coupling between electronic excitations (so-called excitons) and photons confined in a semiconductor cavity grown by molecular beam epitaxy (Fig. 15a). One such cavity, shaped in the form of a micropillar with lateral dimensions of the order of a few microns, behaves like an artificial atom: its discrete energy states (orbitals) are the allowed modes of confined photons (Fig. 15b). By exciting the cavity with a laser beam, the generated electron–hole pairs relax to form polaritons that populate the lowest energy levels. The measurement of the energy and of the angle of the emitted photons allow one to reconstruct the polariton spectrum.

By coupling these cavities to make a honeycomb lattice (Fig. 15-c), one obtains an artificial structure analogue to graphene: the micropillars play the role of carbon atoms, and polaritons which propagate between the pillars play the role of electrons in graphene. The measurement of the dispersion relation of the polaritons by photoluminescence is quite analogous to ARPES experiments in condensed matter. One of the advantages of this system is the possibility to probe the higher orbitals of the pillars, that is the higher energy bands of graphene (Fig. 15-d). These are inaccessible in graphene due to hybridization with higher bands. Here, the lowest two bands of s symmetry are similar to the p_z bands of graphene. The higher energy orbitals, of p_x and p_y symmetry, form four bands with a remarkable structure consisting of two dispersive

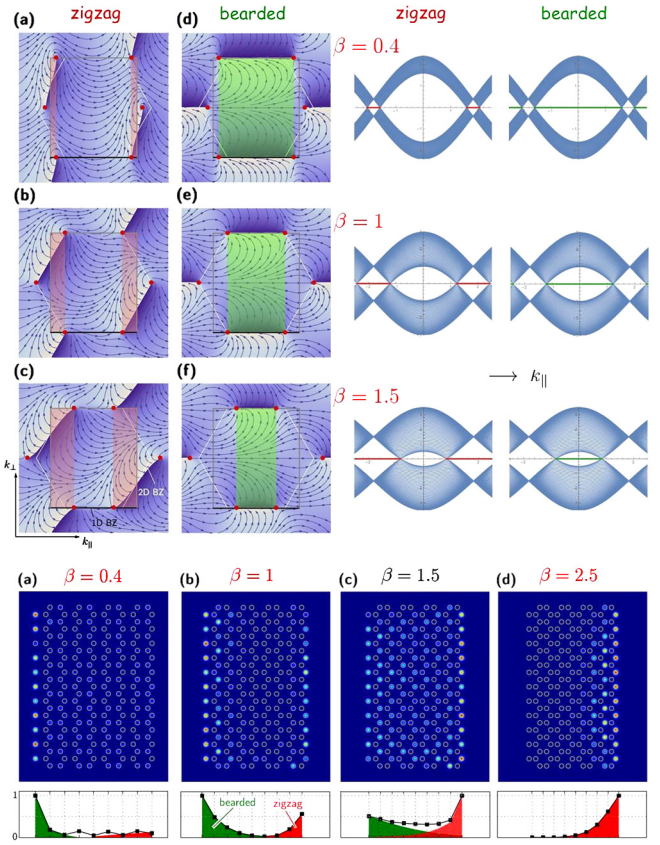

Fig. 14. Top left: winding of the phase $\phi_{\boldsymbol{k}}$ in the Brillouin zone. $w(k_{\|})$, here 0 or 1, measures the number of edges states. There range of existence is colored in pink (zigzag edge states) and green (bearded edge states). Top right: energy spectrum as a function of $k_{\|}$, the wave vector along the direction of the edge. Zero-energy edge states are represented by red and green lines. When β increases, new zigzag states appear at the expense of bearded edge states. This is clearly visible on the experiment (Ref. [32]), which directly measures the intensity of the microwave at the position of each dot.

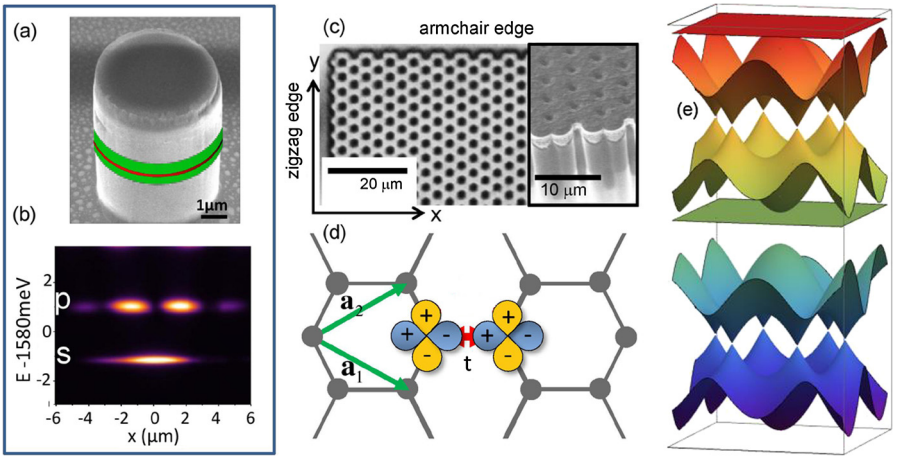

Fig. 15. (a) Polaritons in a micropillar: light is confined in a GaAs cavity (green) where it interacts with quantum-well excitons (red). (b) Photonic states are discrete, like the electronic levels in an atom. (c) Honeycomb lattice of overlapping pillars. Polaritons can propagate in this lattice, like electrons do in graphene. (d) Orbital graphene is obtained by coupling the p_x and p_y states of adjacent sites in the lattice. (e) Band structure exhibiting the p spectrum on top of the s spectrum. The p spectrum resembles the s spectrum, with two additional flat bands (green and red).

bands, which intersect linearly as in graphene, sandwiched between two additional bands that are flat (Figs. 15-e and 19). The s and p dispersion relations have been measured by photoluminiscence and are displayed in Fig. 16.

The p spectrum is well described by a tight-binding model [36]. In the basis of four atomic orbitals (A∞, A∞, B∞, B∞), the 4×4 Hamiltonian has the form (Fig. 17)

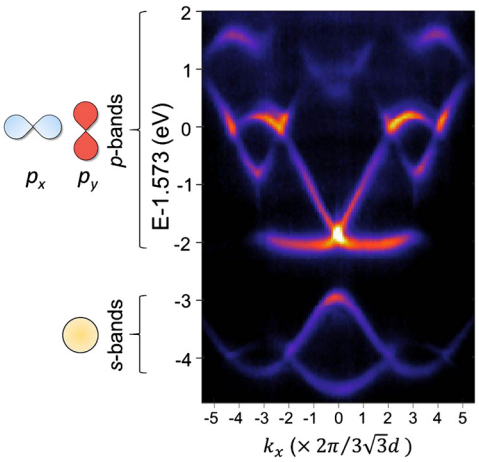

Fig. 16. This photoluminescence spectrum shows the two lowest bands of s symmetry and the higher p bands. The lowest flat band is visible, while the upper flat band is hardly visible because it is hybridized with higher orbitals.

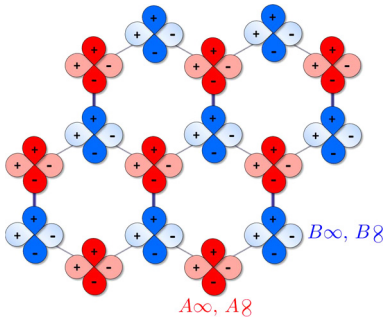

Fig. 17. p_x and p_y orbitals of A and B sites.

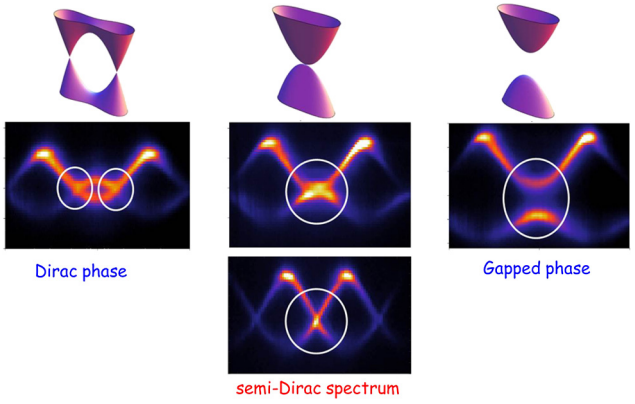

Fig. 18. First direct experimental observation of the merging of Dirac points [37]. At the transition, when $\beta = 2$, the spectrum in the s band is semi-Dirac: it is linear in one direction and it is quadratic in the other direction.

$$\mathcal{H}_{\boldsymbol{k}} = -t \begin{pmatrix} 0 & Q \\ Q^\dagger & 0 \end{pmatrix} \qquad \text{with} \qquad Q = \begin{pmatrix} f_1 & g \\ g & f_2 \end{pmatrix} \tag{30}$$

with $f_1 = \frac{3}{4}(e^{i\boldsymbol{k}\cdot\boldsymbol{a}_1} + e^{i\boldsymbol{k}\cdot\boldsymbol{a}_2})$, $f_2 = \beta + \frac{1}{4}(e^{i\boldsymbol{k}\cdot\boldsymbol{a}_1} + e^{i\boldsymbol{k}\cdot\boldsymbol{a}_2})$ and $g = \frac{\sqrt{3}}{4}(e^{i\boldsymbol{k}\cdot\boldsymbol{a}_1} - e^{i\boldsymbol{k}\cdot\boldsymbol{a}_2})$. The numerical factors account for the overlap of the orbitals when they are not facing each other, see Fig. 17. Under anisotropic strain, the anisotropy of hopping parameters is characterized by the parameter $\beta = t'/t$ that enters the expression of f_2.

This experimental setup is quite rich. The fabrication technique [35] allows one to construct honeycomb lattices with arbitrary strain, well described by an anisotropic tight-binding model. By varying the strain, it has been possible to reach the merging of Dirac points in the s band, and to measure directly for the first time the semi-Dirac dispersion relation, as shown in Fig. 18.

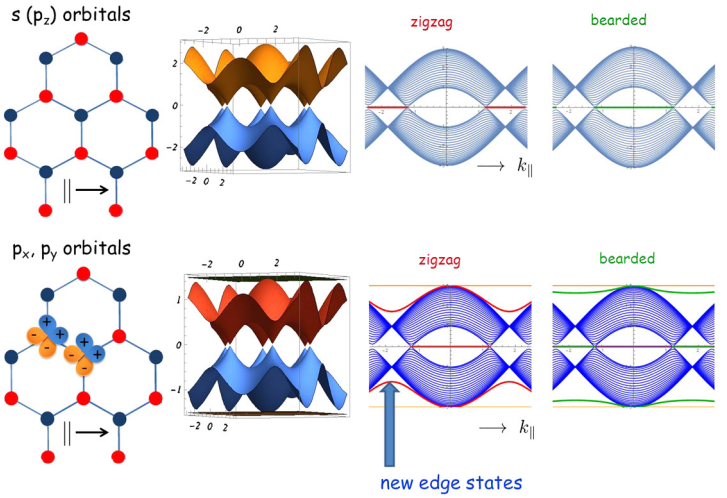

Fig. 19. Comparison of the s and p spectra. The right panels show the dispersion relation along the $k_\perp$ direction parallel to the edges. One sees that the "zero-energy" (middle of the spectrum) states appear at complementary edges (zigzag-bearded), and that new edges states of "finite energy" between the dispersive and the flat bands appear. They have been analyzed in Ref. [38].

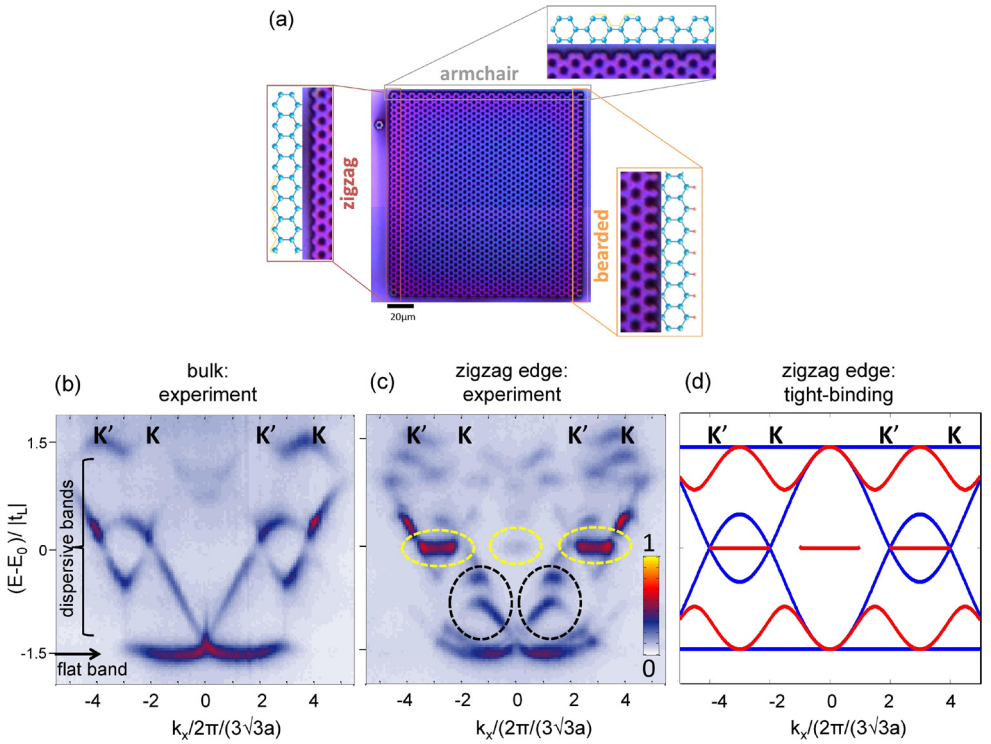

Fig. 20. Top: honeycomb lattice of semiconducting micropillars with three types of edges, zigzag, bearded, and armchair. Bottom: photoluminescence spectrum in the bulk and close to a zigzag edge. The tight-binding spectrum exhibits the zero-energy edge states and new dispersive states (red) between the bulk dispersive states and the flat bands (blue).

The physics of the p spectrum exhibits many new features. Recent experiments have probed the physics of edge states and the evolution of the p spectrum under strain.

Concerning edge states, it was discovered that flat "zero-energy" (in the middle of the p spectrum) edge states exist at positions in momentum space that are complementary to the ones of the s edge states, see Figs. 19 and 20. Additionally, new edge states with dispersive character were found for all types of terminations including armchair. Their theoretically analysis is presented in Ref. [38].

The most recent experiments concern the evolution of the p spectrum under uniaxial strain. Its evolution in the tight-binding model, compared with the one in the s spectrum, is shown in Fig. 21. Several remarkable features have to be

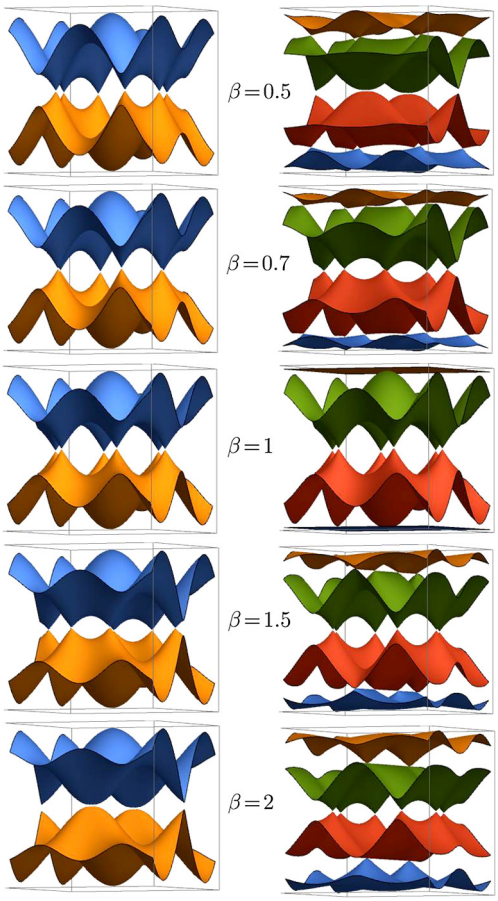

Fig. 21. Compared evolutions of the s and p spectra under applied strain. When $\beta \neq 1$, two Dirac points emerge from the flat band at the Γ point.

discussed. The motion of the Dirac points in the middle of the p spectrum follows an evolution opposite to the one of the s spectrum: merging is reached by *decreasing* the strain parameter $\beta = t'/t$ down to the value $\beta = 0.5$. The flat bands are deformed as soon as $\beta \neq 1$. A remarkable new feature occurs at the quadratic touching point between the dispersive band and the flat band, either at the top or at the bottom of the spectrum. This quadratic touching point characterized by a winding number $w = 2$ splits into a new pair of Dirac points [39]. The scenario of emergence of these points is different from the one described in the above sections where the two Dirac points have *opposite* winding numbers and the merging corresponds to the addition rule of the winding numbers $(+,-) \leftrightarrow 0$. In contrast, the two Dirac points here have the *same winding number*, and the merging/emergence scenario corresponds to addition rule $(+,+) \leftrightarrow 2$ [40–43]. This situation is quite similar to the scenario of splitting of the quadratic touching point observed in bilayer graphene under strain or twist [43,44]. Moreover, these new cones are tilted and, for the first time, a pair of critically tilted cones (that is, is with a vanishing velocity in one direction) has been observed [39].

To finish this section, we wish to mention a remarkable duality between the p spectrum and the s spectrum. The energy bands – flat and dispersive – of the p spectrum, $\epsilon^{\mathrm{p}}_{\mathrm{flat}}$ and $\epsilon^{\mathrm{p}}_{\mathrm{disp}}$ respectively, are related to those of the s spectrum by the remarkable relation derived in Appendix B (consider here only the positive energies, in units of the hopping parameters of the s and p bands):

$$\epsilon^{p}_{\mathrm{flat}}(\beta)\,\epsilon^{p}_{\mathrm{disp}}(\beta) = \frac{3}{4}\beta\,\epsilon_{\mathrm{s}}\left(\frac{1}{\beta}\right) \tag{31}$$

We have named these p bands, "flat" and "dispersive", but note that the upper (lower) band is flat only when $\beta = 1$. From this duality relation, one can draw several conclusions. When $\beta = 1$, the extreme p bands are flat, so that the spectrum of the middle bands is the same as the s spectrum (within renormalization by the hopping parameters). Then one understands immediately the complementarity in the spectra and the edge states described above. A variation of the strain parameter β (β increase or decrease) has *opposite* effects in the p and s spectra. Moreover bearded states in the s band are complementary to the zigzag states in the s band and vice-versa. The wealth of the effects observed in the orbital p band is a motivation for investigation of more sophisticated features in multiband systems.

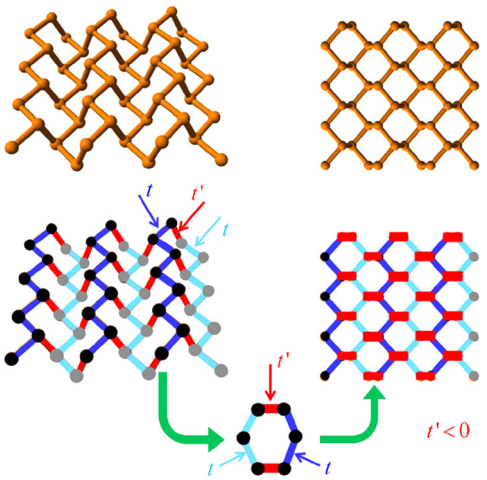

Fig. 22. Like graphene, a 2D crystal of phosphorene may be essentially described by a simple tight-binding model with three hopping integrals t, t, t'. In this case, t' and t have opposite signs. Left: side view, right: top view.

7. Phosphorene

We finally discuss the properties of a condensed matter two-dimensional system that bears strong similarities with graphene. Phosphorene is a two-dimensional crystal in which carbon atoms are replaced by phosphorus atoms. Because of sp^3 hybridization of p orbitals (instead of sp^2 hybridization in graphene), a single sheet of phosphorene is essentially made of two identical planes with horizontal hopping between sites, coupled by an almost vertical hopping (Fig. 22). At ambient pressure, the electronic spectrum is gapped around the Γ point, but under pressure or vertical strain, a pair of Dirac points emerges from this point [45,46]. We show here that this transition follows the scenario of the universal Hamiltonian (20). Although sophisticated large-scale tight-binding simulations have been developed with up to nine parameters [47,48], their basic features are captured within our simple toy model with the two parameters of t, t', which is used for strained graphene and which is also relevant here.

We have shown above that the merging parameter Δ_* depends on the position of the merging/emergence TRIM point and is given by

$$\Delta_* = t' + (-1)^p t + (-1)^q t \tag{32}$$

In graphene and the realizations discussed above, the two parameters are positive, the transition occurs at the M_2 point so that the relevant combination is $\Delta_* = t' - 2t$. In graphene, $t' = t$, so that this parameter is negative. Under strain, t' increases, so that Δ_* becomes positive and this happens at the topological transition.

In phosphorene, at ambient pressure, the hopping parameters t and t' have opposite signs: $t > 0$ and $t' < 0$. The spectrum is gapped, which means that $\Delta_* > 0$. Under pressure or vertical strain, the Dirac points emerge at the Γ point ($p = q = 0$), and this phenomenon is therefore driven by the parameter $\Delta_* = t' + 2t$, which becomes negative. The reason is that the amplitude of negative t' increases under pressure. This emergence of Dirac points is very well described by the universal Hamiltonian. The calculated evolution of the Landau level spectrum in a complete tight-binding description of phosphorene is quite similar to the expected spectrum obtained from the universal Hamiltonian (compare Fig. 7 and figure 7 of Ref. [49]).

The two scenarios of merging or emergence in graphene-like structure and phosphorene are summarized in Fig. 23. We conclude that the merging/emergence of Dirac points in strain (artificial graphene) or phosphorene follows the same universal scenario.

8. Conclusion

We have described several physical systems where the excitation spectrum exhibits a pair of Dirac cones, such as graphene. The flexibility of these different systems allows one to vary hopping parameters so that these Dirac points can be manipulated: they can move, merge or emerge at special points of high symmetry of the reciprocal lattice.

Each Dirac point is characterized by a winding number $w = \pm 1$, and a pair of Dirac points can merge following two alternative scenarios: either they have opposite "charges" and this corresponds to the scenario discussed in this paper, $(+-) \leftrightarrow 0$, or they have identical charge and this corresponds to a second merging scenario, $(++) \leftrightarrow 2$, described by another effective Hamiltonian, and which is not discussed in this paper. For a discussion on this second scenario, see the references [50,51]. The merging between two Dirac cones is thus a topological transition that may be described by two distinct universality classes, according to whether the two cones have opposite or identical topological charges. We have

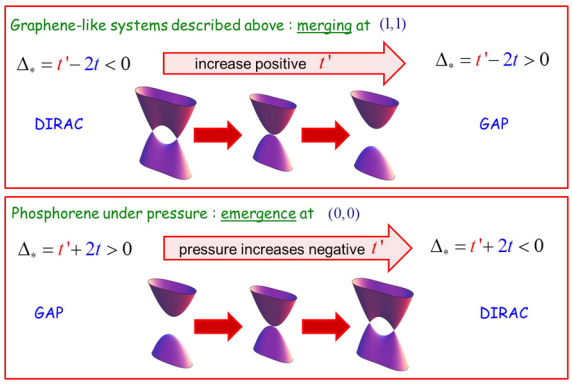

Fig. 23. Similarly to graphene, a 2D crystal of phosphorene may be essentially described by a simple tight-binding model with three hopping integrals t, t, t'. In this case, t' and t have opposite signs.

recently found a system in which the two classes may be observed: indeed, photoluminescence experiments on the p spectrum of a strained honeycomb polariton lattice have shown a very rich variety of Dirac points. Both types of merging have been observed [39]. In particular, we have highlighted the existence of a pair of Dirac points emerging from the touching point between a quadratic band and a flat band, following the scenario $(+,+) \leftrightarrow 2$. It turns out that under further strain, this pair of Dirac points may merge at another TRIM following the scenario $(+,-) \leftrightarrow 0$ [39,52]. This apparent contradiction is solved by the fact that the winding number is actually defined around a unit vector on the Bloch sphere and that this vector rotates during the motion of the Dirac points [52]. These new results open the way for future investigations on the production of Dirac points, their geometric properties and their fate under appropriate variations of external parameters, especially in multiband systems.

Acknowledgements

This work has benefited from collaborations and discussions with A. Amo, M. Bellec, C. Bena, J. Bloch, P. Delplace, R. de Gail, P. Dietl, J.-N. Fuchs, M.-O. Goergig, U. Kuhl, L.-K. Lim, M. Milićević, F. Mortessagne, T. Ozawa, F. Piéchon, D. Ullmo. Special thanks to J.-N. Fuchs and M.-O. Goergig for a careful rereading of the manuscript.

Appendix A. A remark on two representations of a Bloch function

In the tight-binding picture, the eigenstates, solutions to the Hamiltonian (1), are a combination of atomic orbitals satisfying Bloch's theorem. They can be written in the alternative forms [53]

$$|\psi_{\boldsymbol{k}}\rangle = \frac{1}{\sqrt{N}} \sum_j \mathrm{e}^{\mathrm{i}\boldsymbol{k}\cdot\boldsymbol{R}_j} \left(c^{\mathrm{A}}_{\boldsymbol{k}} |\varphi^{\mathrm{A}}_j\rangle + c^{\mathrm{B}}_{\boldsymbol{k}} |\varphi^{\mathrm{B}}_j\rangle \right) \tag{33}$$

or

$$|\psi_{\boldsymbol{k}}\rangle = \frac{1}{\sqrt{N}} \sum_j \left(\mathrm{e}^{\mathrm{i}\boldsymbol{k}\cdot\boldsymbol{R}^{\mathrm{A}}_j} d^{\mathrm{A}}_{\boldsymbol{k}} |\varphi^{\mathrm{A}}_j\rangle + \mathrm{e}^{\mathrm{i}\boldsymbol{k}\cdot\boldsymbol{R}^{R}_j} d^{\mathrm{B}}_{\boldsymbol{k}} |\varphi^{\mathrm{B}}_j\rangle \right) \tag{34}$$

where φ^{A}_j and φ^{B}_j are atomic orbitals on sites (j, A) and (j, B)). This is the same eigenstate, but these two representations are slightly different. In the first expression, the phase factor in attached to the elementary cell and is common to the A and B sites. This is, for example, the form found in the Ashcroft and Mermin book (eq. 10.26) [54]. In the second writing, each phase factor is attached to the position of each atom, A or B. This is, for example, the notation found in the Wallace paper [55]. By choosing $\boldsymbol{R}_j = \boldsymbol{R}^{\mathrm{A}}_j$, we have obviously $c^{\mathrm{A}}_{\boldsymbol{k}} = d^{\mathrm{A}}_{\boldsymbol{k}}$ and $c^{\mathrm{B}}_{\boldsymbol{k}} = d^{\mathrm{B}}_{\boldsymbol{k}} \mathrm{e}^{\mathrm{i}\boldsymbol{k}\cdot(\boldsymbol{R}^{\mathrm{B}} - \boldsymbol{R}^{\mathrm{A}})} = d^{\mathrm{B}}_{\boldsymbol{k}} \mathrm{e}^{\mathrm{i}\boldsymbol{k}\cdot\delta_3}$, δ_3 being the A–B distance (Fig. 2). The two representations of the same eigenfunction are of the form

$$\psi(\boldsymbol{r}) = \mathrm{e}^{\mathrm{i}\boldsymbol{k}\cdot\boldsymbol{R}}\, u_{\mathrm{I},\boldsymbol{k}}(\boldsymbol{r}) \tag{35}$$

$$\psi(\boldsymbol{r}) = \mathrm{e}^{\mathrm{i}\boldsymbol{k}\cdot\boldsymbol{r}}\, u_{\mathrm{II},\boldsymbol{k}}(\boldsymbol{r}) \tag{36}$$

where $\boldsymbol{r}$ is the position and $\boldsymbol{R}$ is a vector of the Bravais lattice, position of the elementary cell in the lattice. Note that the function $u_{\mathrm{I},\boldsymbol{k}}(\boldsymbol{r})$ has the periodicity of the reciprocal lattice, while $u_{\mathrm{II},\boldsymbol{k}}(\boldsymbol{r})$, which is the most common representation, does not.

In the tight-binding model (1), the wave function is defined only on the A and B sites so that the normalized wave functions can be written in the spinorial form:

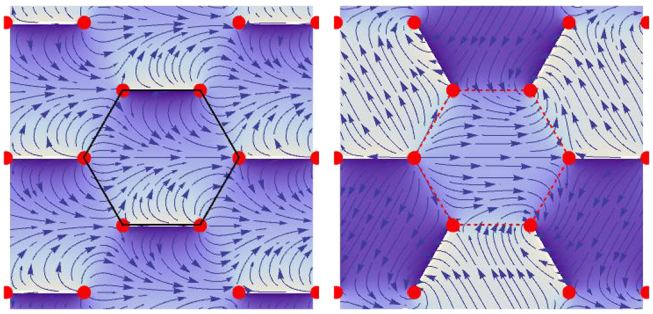

Fig. 24. Representation of the phases $\phi_{\mathrm{I},\boldsymbol{k}}$ (left) and $\phi_{\mathrm{II},\boldsymbol{k}}$ (right), via the vector field $(\cos\phi, \sin\phi)$. The phase $\phi_{\mathrm{I},\boldsymbol{k}}$ has the periodicity of the reciprocal lattice. The phase $\phi_{\mathrm{II},\boldsymbol{k}}$ has a triple periodicity. This phase has been measured directly in interferometry experiments with a honeycomb lattice of cold atoms [27–29] and in ARPES experiments on graphene (Fig. 26) [56].

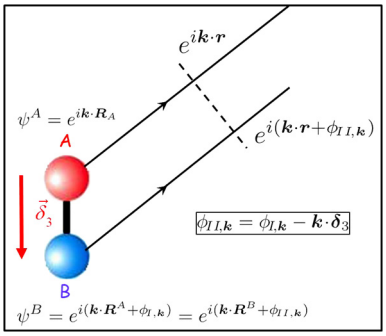

Fig. 25. The waves emitted by the sites of the honeycomb lattice can be described by a "two-source" interference pattern [56].

$$\text{either} \qquad u_{\mathrm{I},\boldsymbol{k}} = \begin{pmatrix} c^{\mathrm{A}}_{\boldsymbol{k}} \\ c^{\mathrm{B}}_{\boldsymbol{k}} \end{pmatrix} = \frac{1}{\sqrt{2}} \begin{pmatrix} 1 \\ \pm \mathrm{e}^{\mathrm{i}\phi_{\mathrm{I},\boldsymbol{k}}} \end{pmatrix} \tag{37}$$

$$\text{or} \qquad u_{\mathrm{II},\boldsymbol{k}} = \begin{pmatrix} d^{\mathrm{A}}_{\boldsymbol{k}} \\ d^{\mathrm{B}}_{\boldsymbol{k}} \end{pmatrix} = \frac{1}{\sqrt{2}} \begin{pmatrix} 1 \\ \pm \mathrm{e}^{\mathrm{i}\phi_{\mathrm{II},\boldsymbol{k}}} \end{pmatrix} \tag{38}$$

They are solutions to the 2×2 Hamiltonian

$$\mathcal{H}_{i,\boldsymbol{k}} = \begin{pmatrix} 0 & f_{i,\boldsymbol{k}} \\ f^*_{i,\boldsymbol{k}} & 0 \end{pmatrix} \tag{39}$$

with

$$\text{either} \qquad f_{\mathrm{I},\boldsymbol{k}} = -t(1 + \mathrm{e}^{\mathrm{i}\boldsymbol{k}\cdot\boldsymbol{a}_1} + \mathrm{e}^{\mathrm{i}\boldsymbol{k}\cdot\boldsymbol{a}_2}) \tag{40}$$

$$\text{or} \qquad f_{\mathrm{II},\boldsymbol{k}} = -t(\mathrm{e}^{\mathrm{i}\boldsymbol{k}\cdot\boldsymbol{\delta}_3} + \mathrm{e}^{\mathrm{i}\boldsymbol{k}\cdot\boldsymbol{\delta}_1} + \mathrm{e}^{\mathrm{i}\boldsymbol{k}\cdot\boldsymbol{\delta}_2}) \tag{41}$$

and the relative phase between the two components of the wave function is given by $\phi_{i,\boldsymbol{k}} = \arg(f^*_{i,\boldsymbol{k}})$, so that

$$\phi_{\mathrm{II},\boldsymbol{k}} = \phi_{\mathrm{I},\boldsymbol{k}} - \boldsymbol{k}\cdot\boldsymbol{\delta}_3 \tag{42}$$

In the first representation, the phase $\phi_{\mathrm{I},\boldsymbol{k}}$ has the periodicity of the reciprocal lattice: $\phi_{\mathrm{I},\boldsymbol{k}+\boldsymbol{G}} = \phi_{\mathrm{I},\boldsymbol{k}}$, see Fig. 24. Obviously, because of the linear term $\boldsymbol{k}\cdot\boldsymbol{\delta}_3$ related to the A–B distance, the phase $\phi_{\mathrm{II},\boldsymbol{k}}$ does not have this periodicity, but a triple periodicity (Fig. 24).

What is the physical interpretation of these two phases ϕ_{I} and ϕ_{II}? The periodic honeycomb lattice can be represented by a two-source emitter [56] corresponding to the two sublattices, see Fig. 25. $\phi_{\mathrm{I},\boldsymbol{k}}$ is the relative phase between the two emitters, that is, the phase delay between the waves emitted by the two sites. It does not account for the relative position between these two sites. If $\boldsymbol{k}\cdot\boldsymbol{r}$ represents the phase emitted by atoms A at any point $\boldsymbol{r}$, the combination $\boldsymbol{k}\cdot\boldsymbol{r} + \phi_{\mathrm{II},\boldsymbol{k}}$ represents the phase emitted by atoms B at the same point (Fig. 25). The signals emitted by the two sources construct an interference pattern that depends on the relative position between the two sources. At a position $\boldsymbol{r}$ outside the sample, the total electronic wave has the form $\mathrm{e}^{\mathrm{i}\boldsymbol{k}\cdot(\boldsymbol{r}-\boldsymbol{R}_{\mathrm{A}})}\psi_{\mathrm{A}} + \mathrm{e}^{\mathrm{i}\boldsymbol{k}\cdot(\boldsymbol{r}-\boldsymbol{R}_{\mathrm{B}})}\psi_{\mathrm{B}} = (1 + \mathrm{e}^{\mathrm{i}\phi_{\mathrm{II},\boldsymbol{k}}})\mathrm{e}^{\mathrm{i}\boldsymbol{k}\cdot\boldsymbol{r}}$, so that the intensity $I(\boldsymbol{k})$ is proportional to $\cos^2\frac{\phi_{\mathrm{II},\boldsymbol{k}}}{2}$, as measured in ARPES experiments, see Fig. 26.

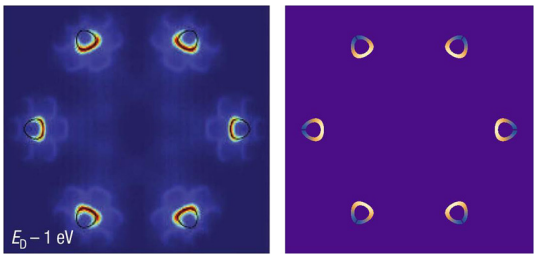

Fig. 26. Left: ARPES measured intensity [56]. Right: intensity given by $\cos^2 \frac{\phi_{\mathrm{II},\boldsymbol{k}}}{2}$.

In this paper, we have used the representation I for the writing of the Hamiltonian (4) in its general form (14), which has the periodicity of the reciprocal lattice. It is also used for describing the geometric properties of the Hamiltonian and the wave functions, the relation between the existence of edge states and the Zak phase [33]. The phase $\phi_{\mathrm{II},\boldsymbol{k}}$ is directly measured in interferometry experiments on cold atoms [27–29] or in ARPES experiments [56], because the interference pattern depends on the relative position $\boldsymbol{\delta}_3$ between atoms A and B. This phase does not have the periodicity of the reciprocal lattice.

Appendix B. Proof of Eq. (31)

This equation relates the dispersion relation of the p bands to the dispersion relation of the s band. The p spectrum consists in four bands of energies named $\pm\epsilon_{\mathrm{flat}}$ and $\pm\epsilon_{\mathrm{disp}}$. Note that the two "flat" bands are strictly flat only when $\beta = 1$.

Consider first the s spectrum. It is given by $\pm\epsilon_s(\beta)$ with $\epsilon_s(\beta) = |f_{\boldsymbol{k}}|$, where $f_{\boldsymbol{k}}$ is given by Eq. (12). Therefore in units of t, it can be written as

$$\epsilon_s(\beta) = |\beta + z_1 + z_2| \tag{43}$$

where $z_i = e^{i\boldsymbol{k}\cdot\boldsymbol{a}_i}$.

Consider now the eigenvalues of the p-Hamiltonian (30). Simple algebra shows that the eigenvalues are solutions to the equation

$$\epsilon^4 - S\epsilon^2 + P = 0 \tag{44}$$

with

$$S = \mathrm{tr}(Q\,Q^\dagger) \quad , \quad P = \det(Q\,Q^\dagger) = |\det Q\,|^2 \tag{45}$$

so that

$$\epsilon^p_{\mathrm{flat}}\,\epsilon^p_{\mathrm{disp}} = |\det Q\,| \tag{46}$$

Writing the elements of the matrix Q as $f_1 = \frac{3}{4}(z_1 + z_2)$, $f_2 = \beta + \frac{1}{4}(z_1 + z_2)$ and $g = \frac{\sqrt{3}}{4}(z_1 - z_2)$, we find

$$\begin{aligned}\epsilon^p_{\mathrm{flat}}(\beta)\,\epsilon^p_{\mathrm{disp}}(\beta) &= \frac{3}{4}\beta\left|\frac{z_1 z_2}{\beta} + z_1 + z_2\right| \\ &= \frac{3}{4}\beta\left|\frac{1}{\beta} + z_1 + z_2\right|\end{aligned} \tag{47}$$

since $|z_i| = 1$. This proves Eq. (31).

References

[1] A.K. Geim, K.S. Novoselov, Nat. Mater. 6 (2007) 183.
[2] For a review, see A.H. Castro Neto, N.M.R. Peres, K.S. Novoselov, A.K. Geim, Rev. Mod. Phys. 81 (2009) 109.
[3] D. Matter, Poincaré Seminar, Prog. Math. Phys. 71 (2016).
[4] G. Montambaux, F. Piéchon, J.-N. Fuchs, M.-O. Goerbig, Phys. Rev. B 80 (2009) 153412, Eur. Phys. J. B 72 (2009) 509.
[5] V.M. Pereira, A.H. Castro Neto, N.M.R. Peres, Phys. Rev. B 80 (2009) 045401.
[6] M.-O. Goerbig, J.-N. Fuchs, G. Montambaux, F. Piéchon, Phys. Rev. B 78 (2008) 045415.
[7] M. Polini, F. Guinea, M. Lewenstein, H.C. Manoharan, V. Pellegrini, Nat. Nanotechnol. 8 (2013) 625.
[8] G. Volovik, The Universe in a Helium Droplet, Oxford University Press, 2009.
[9] For a discussion between frequent confusion between the winding number and the Berry phase, see C.-H. Park, N. Marzari, Phys. Rev. B 84 (2011) 205440.
[10] L. Onsager, Philos. Mag. 43 (1952) 1006;
I.M. Lifshitz, A.M. Kosevich, Sov. Phys. JETP 2 (1956) 636.

[11] L. Roth, Phys. Rev. B 145 (1966) 434.
[12] J.-N. Fuchs, F. Piéchon, G. Montambaux, M.-O. Goerbig, Eur. Phys. J. B 77 (2010) 351.
[13] Y. Zhang, Y.-W. Tan, H.L. Stormer, P. Kim, Nature 438 (2005) 201.
[14] Y. Hasegawa, R. Konno, H. Nakano, M. Kohmoto, Phys. Rev. B 74 (2006) 033413.
[15] P. Dietl, F. Piéchon, G. Montambaux, Phys. Rev. Lett. 100 (2008) 236405.
[16] B. Wunsch, F. Guinea, F. Sols, New J. Phys. 10 (2008) 103027.
[17] V. Pardo, W.E. Pickett, Phys. Rev. Lett. 102 (2009) 166803;
S. Banerjee, R.R.P. Singh, V. Pardo, W.E. Pickett, Phys. Rev. Lett. 103 (2009) 016402.
[18] P. Adroguer, D. Carpentier, G. Montambaux, E. Orignac, Phys. Rev. B 93 (2016) 125113.
[19] A. Kobayashi, S. Katayama, Y. Suzumura, Sci. Technol. Adv. Mater. 10 (2009) 024309;
A. Kobayashi, Y. Suzumura, F. Piéchon, G. Montambaux, Phys. Rev. B 84 (2011) 075450.
[20] L. Tarruell, D. Greif, T. Uehlinger, G. Jotzu, T. Esslinger, Nature 483 (2012) 302.
[21] F. Bloch, Z. Phys. 52 (1929) 555.
[22] M. Dahan, E. Peik, J. Reichel, Y. Castin, C. Salomon, Phys. Rev. Lett. 76 (1996) 4508.
[23] L.D. Landau, Phys. Z. Sowjetunion 2 (1932) 46;
C. Zener, Proc. R. Soc. Lond. Ser. A 137 (1932) 696;
See also C. Wittig, J. Phys. Chem. B 109 (2005) 8428.
[24] L.-K. Lim, J.-N. Fuchs, G. Montambaux, Phys. Rev. Lett. 108 (2012) 175303;
J.-N. Fuchs, L.-K. Lim, G. Montambaux, Phys. Rev. A 86 (2012) 063613.
[25] S.N. Shevchenko, S. Ashhab, F. Nori, Phys. Rep. 492 (2010) 1.
[26] L.-K. Lim, J.-N. Fuchs, G. Montambaux, Phys. Rev. Lett. 112 (2014) 155302, Phys. Rev. A 91 (2015) 042119.
[27] T. Li, L. Duca, M. Reitter, F. Grust, E. Demler, M. Endres, M. Schleier-Smith, I. Bloch, U. Schneider, Science 352 (2016) 1094.
[28] M. Tarnowski, M. Nuske, N. Fläschner, B. Rem, D. Vogel, L. Freystatzky, K. Sengstock, L. Mathey, C. Weitenberg, Phys. Rev. Lett. 118 (2017) 240403.
[29] L.-K. Lim, J.-N. Fuchs, G. Montambaux, Phys. Rev. A 92 (2015) 063627.
[30] M. Bellec, U. Kuhl, G. Montambaux, F. Mortessagne, Phys. Rev. Lett. 110 (2013) 033902.
[31] M. Bellec, U. Kuhl, G. Montambaux, F. Mortessagne, Phys. Rev. B 88 (2013) 115437.
[32] M. Bellec, U. Kuhl, G. Montambaux, F. Mortessagne, New J. Phys. 16 (2014) 113023.
[33] P. Delplace, D. Ullmo, G. Montambaux, Phys. Rev. B 84 (2011) 195452.
[34] M.C. Rechtsman, Y. Plotnik, J.M. Zeuner, A. Szameit, M. Segev, Phys. Rev. Lett. 111 (2013) 103901.
[35] T. Jacqmin, I. Carusotto, I. Sagnes, M. Abbarchi, D. Solnyshkov, G. Malpuech, E. Galopin, A. Lemaître, J. Bloch, A. Amo, Phys. Rev. Lett. 112 (2014) 116402.
[36] C. Wu, D. Bergman, L. Balents, S. Das Sarma, Phys. Rev. Lett. 99 (2007) 070401.
[37] M. Milićević, et al., in preparation.
[38] M. Milićević, T. Ozawa, G. Montambaux, I. Carusotto, E. Galopin, A. Lemaître, L. Le Gratiet, I. Sagnes, J. Bloch, A. Amo, Phys. Rev. Lett. 118 (2017) 107403.
[39] M. Milićević, G. Montambaux, T. Ozawa, I. Sagnes, A. Lemaître, L. Le Gratiet, A. Harouri, J. Bloch, A. Amo, arXiv:1807.08650.
[40] Y.D. Chong, X.-G. Wen, M. Soljačić, Phys. Rev. B 77 (2008) 235125.
[41] K. Sun, H. Yao, E. Fradkin, S.A. Kivelson, Phys. Rev. Lett. 103 (2009) 046811.
[42] B. Dora, I.F. Herbut, R. Moessner, Phys. Rev. B 90 (2014) 045310.
[43] R. de Gail, M.O. Goerbig, F. Guinea, G. Montambaux, A.H. Castro Neto, Phys. Rev. B 84 (2011) 045436.
[44] E. McCann, V.I. Fal'ko, Phys. Rev. Lett. 96 (2006) 086805.
[45] J. Kim, S.S. Baik, S.H. Ryu, Y. Sohn, S. Park, B.-G. Park, J. Denlinger, Y. Yi, H.J. Choi, K.S. Kim, Science 349 (2015) 723.
[46] An applied electric field may also drive this transition. The evolution of the electronic spectrum in a field has been observed directly by ARPES measurements. Z.J. Xiang, G.J. Ye, C. Shang, B. Lei, N.Z. Wang, K.S. Yang, D.Y. Liu, F.B. Meng, X.G. Luo, L.J. Zou, Z. Sun, Y. Zhang, X.H. Chen, Phys. Rev. Lett. 115 (2015) 186403.
[47] M. Ezawa, New. J. Phys. 16 (2014) 115004.
[48] A.N. Rudenko, S. Yuan, M.I. Katsnelson, Phys. Rev. B 92 (2015) 085419.
[49] J.M. Pereira, M.I. Katsnelson, Phys. Rev. B 92 (2015) 075437.
[50] R. de Gail, J.-N. Fuchs, M.O.G.F. Piéchon, G. Montambaux, Physica B 407 (2012) 1948;
R. de Gail, M.O. Goerbig, G. Montambaux, Phys. Rev. B 86 (2012) 045407.
[51] For a review, see M.O. Goerbig, G. Montambaux, Dirac Matter, Poincaré Seminar, Prog. Math. Phys. 71 (2016) 25.
[52] G. Montambaux, L.-K. Lim, J.-N. Fuchs, F. Piéchon, arXiv:1804.00781.
[53] C. Bena, G. Montambaux, New J. Phys. 11 (2009) 095003.
[54] N.W. Ashcroft, N.D. Mermin, Solid State Physics, Saunders, Philadelphia, 1976.
[55] P.R. Wallace, Phys. Rev. 71 (1947) 622.
[56] M. Mucha-Kruczynski, O. Tsyplyatev, A. Grishin, E. McCann, V.I. Fal'ko, A. Bostwick, E. Rotenberg, Phys. Rev. B 77 (2008) 195403.